RSC Advances

PAPER

Check for updates

Cite this: *RSC Adv.*, 2021, **11**, 33481

Construction of 1T@2H MoS_2 heterostructures *in situ* from natural molybdenite with enhanced electrochemical performance for lithium-ion batteries†

ChengLong Peng, Mingming Shi, Fei Li, Yang Wang, Xueqin Liu, HuaSheng Liu and Zhen Li *

Natural molybdenite, an inexpensive and naturally abundant material, can be directly used as an anode material for lithium-ion batteries. However, how to release the intrinsic capacity of natural molybdenite to achieve high rate performance and high capacity is still a challenge. Herein, we introduce an innovative, effective, and one-step approach to preparing a type of heterostructure material containing 1T@2H MoS_2 crafted from insertion and expansion of natural molybdenite. The metallic 1T phase formed *in situ* can significantly improve the electronic conductivity of MoS_2. At the same time, 1T@2H MoS_2 heterostructures can provide an internal electric field (E-field) to accelerate the migration rate of electrons and ions, promote the charge transfer behaviour, and ensure the reaction reversibility and lithium storage kinetics. Such worm-like 1T@2H MoS_2 heterostructures also have a large specific surface area and a large number of defects, which will help shorten the lithium-ion transmission distance and provide more ion transmission channels. As a result, it exhibits a discharge capacity of 788 mA h g^{-1} remarkably at 100 mA g^{-1} after 485 cycles and stable cycling performance. It also shows excellent magnification performance of 727 mA h g^{-1} at 1 A g^{-1}, compared to molybdenite concentrate. Briefly, this work's heterostructure architectures open up a new avenue for applying natural molybdenite in lithium-ion batteries, which has the potential to achieve large-scale commercial applications.

Received 20th July 2021
Accepted 28th September 2021

DOI: 10.1039/d1ra05565h

rsc.li/rsc-advances

Introduction

As one of the most critical energy storage systems, lithium-ion batteries (LIBs) have advanced energy storage and conversion systems. Exploring electrode materials with functional electrochemical performance and large-scale application is the current research hotspot.[1,2] Transition metal sulfides have been considered as promising anode materials for LIBs because of their graphite-like layered structure, adjustable interlayer distance and bandgap, diverse composition, and good electrochemical reversibility in their high specific capacity. Among them, MoS_2, as the most representative, has a higher theoretical capacity (669 mA h g^{-1}) and a larger interlayer spacing (0.615 nm), which can achieve rapid transmission of alkali metal ions. Meanwhile, the capacity of MoS_2 in actual research can even be as high as 1000 mA h g^{-1}. Mo atoms can accommodate a large number of Li ions in the cycle process, which can provide additional capacity.[3] The high lithium storage mechanism facilitates the development of energy storage equipment with high capacity and power density.

So far, MoS_2 are synthesized by chemical methods in most studies, such as hydrothermal,[4] chemical vapor deposition,[5] solvothermal,[6,7] other way,[8–10] *etc.* Although the above chemical synthesis methods can prepare MoS_2 on a large scale, their industrial application is still limited by strict reaction conditions and environmental pollution. In nature, MoS_2 exists in the form of natural molybdenite and is generally obtained by physical purification. Therefore, preparing MoS_2 material directly from natural molybdenite concentrate can eliminate many intermediate complex steps and reduce synthetic pollutants. Compared with synthetic MoS_2, natural molybdenite also has the advantages of abundant resources and low cost, which makes it become a potential candidate of commercial energy storage material for sustainable development. Unfortunately, during the charging and discharging process of natural molybdenite and synthetic MoS_2, the active material will be crushed and loosely contacted due to their low internal electronic conductivity and significant volume changes, and eventually leads to rapid capacity degradation.[11,12] Improving the electronic conductivity of MoS_2 to achieve its high capacity and cycle stability is still a challenge. There are roughly two general

Engineering Research Center of Nano-Geomaterials of Ministry of Education, Faculty of Materials Science and Chemistry, China University of Geosciences, Wuhan 430074, China. E-mail: zhenli@cug.edu.cn

† Electronic supplementary information (ESI) available. See DOI: 10.1039/d1ra05565h

This article is licensed under a Creative Commons Attribution-NonCommercial 3.0 Unported Licence.

(cc) BY-NC

© 2021 The Author(s). Published by the Royal Society of Chemistry

strategies to overcome the issues: (1) composite with carbon-based materials to improve the material's electrical conductivity, such as MoS_2/graphite heterostructures, or with graphene to form MoS_2@C@RGO composites.[12,13] However, this strategy also has drawbacks such as complex processes, high cost, and reduced specific capacity; (2) accomplish few layers through the insertion/exfoliation method, which will effectively shorten the transmission distance of lithium ions and ensure transmission efficiency.[11,14] Simultaneously, a part of the triangular 2H phase usually transforms into the octahedral 1T phase during the insertion/exfoliation process to make Mo and S coordinate differently, giving it a different electronic structure. Noted, because of its metallicity (10^7 times more conductive than 2H), hydrophilicity, and larger layer spacing, 1T MoS_2 can be used in lithium-ion batteries to effectively reduce charge transfer resistance and accelerate the ion transfer rate.[15–18] In recent research, the chemical intercalation exfoliation[19] and electrochemical intercalation exfoliation[20] would have realized the few layers and crystal phase transformation of bulky MoS_2. Still, it has drawbacks, including complex processes, low yield, low tap density, and easy aggregation of the nanostructures. Therefore, we need a simple design that can guarantee the bulky natural molybdenite's advantages of high tap density and non-agglomeration, improve its electronic conductivity, release its inherent capacity, and achieve high rate performance.

To better resolve the issues, we designed a MoS_2 heterostructures anode material composed of abundant 1T MoS_2 and 2H MoS_2 (denoted as 1T@2H MoS_2). The 1T@2H MoS_2 heterostructures were fabricated by a novel and simple expansion method. Due to its metallic properties, 1T MoS_2 synthesized *in situ* from natural molybdenite could enhance its electrical conductivity and decrease the kinetic barrier.[17] The 1T@2H MoS_2 heterostructures generated an internal E-field, dramatically accelerating the migration rate of ions and electrons and improved the reaction kinetics. Simultaneously, the natural molybdenite was worm-like, which retained the high tap density of the bulk material, which significantly increased the specific surface areas and pore volumes, and provided more ion channels and exposed active sites. Since there is enough void space between the adjacent layers of MoS_2, a worm-like structure is beneficial to accommodate the volume change during the intercalation of lithium ions. Furthermore, 1T MoS_2 and the designed E-field can initially solve carriers' transport, electrons transfer, and ions diffusion in the dense MoS_2 structure. As a result, the worm-like 1T@2H MoS_2 heterostructures had higher electronic conductivity and Li^+ diffusion rate than natural molybdenite, indicating a higher specific capacity, good cycle stability, and excellent magnification performance. 1T@2H MoS_2 heterostructures will improve the lithium storage performance. All these features make it a promising material for practical application.

Experimental section

Preparation of 1T@2H MoS_2

All the reagents were purchased from Sinopharm and used without other purification. Molybdenite concentrate (MoS_2 content: ~78%, Luanchuan City, Henan Province, China) was obtained from raw ore through flotation and grinding. In the experiment, 1T@2H MoS_2 heterostructures were received by the expansion method. Molybdenite concentrate (1.5 g), sodium hydroxide (20 g), hydrazine hydrate (20 mL, wt% = 85%), and magnetons were sealed in a PTFE autoclave, heated, and stirred in an oil bath at 150 °C for 24 h. The bulky molybdenite concentrate was put into the autoclave at 150 °C and stirred by magnetic force. The worm-like 1T@2H MoS_2 was washed with deionized water and ethanol until it was neutral. Finally, the samples were placed in an oven at 60 °C overnight to obtain 1T@2H MoS_2. The reaction temperature, reaction time, and the concentration of sodium hydroxide all have essential effects on the worm-like 1T@2H MoS_2 heterostructures. Table S1† listed the different reaction conditions such as reaction temperature, reaction time, and sodium hydroxide concentration to prepare 1T@2H MoS_2 heterostructures.

Characterization

Crystal structures were measured using X-ray diffraction (XRD, Bruker AXS D8 Advance) with Cu K radiation (=1.5406 Å) in a scan range of 5–70°. The element contents of the sample were analyzed by X-ray fluorescence (XRF, XRF-AXIOSmax). Raman (ThermoFisher Scientific) was a non-destructive and effective method for collecting sample structure and molecular rotation information with a test range of 400–4000 cm^{-1}. The morphology and microstructure of the samples were characterized by HITACHI SU8010 scanning field-emission electron microscope (FESEM). A transmission electron microscope (TEM, JEOL 2100), high-resolution (HRTEM), and scanning transmission electron microscopy (STEM) was used to observe the fine structure of the samples. X-ray photoelectron spectroscopy (XPS, Thermo Scientific, Al K_α X-ray) equipped with Al K_α X-ray source was used to study the sample's chemical state and valence state. The diffuse reflection spectra of ultraviolet-visible (UV-Vis) were investigated by Shimadzu UV-2600 spectrophotometer. N_2 adsorption and desorption isotherm (BET, ASAP2460) was used to measure the sample's specific surface area and pore size distribution characteristics. The BT-9300ST laser particle size analyzer analyzed the particle size of the samples. A four-probe tester (RTS-9, $10^{-5} \sim 10^5$ S cm^{-1}) measured the electronic conductivity of the model.

Electrochemical measurement

During the battery test, the active substance, conductive agent acetylene black, and binder sodium alginate were mixed in an aqueous solution at a mass ratio of 7 : 2 : 1 to prepare the working electrode. Then the slurry mixture was uniformly coated on the copper foil. Finally, the powder-coated copper foil was placed in a vacuum oven at 80 °C for 12 hours and used as the final working electrode. The mass density of the active material of each electrode sheet is 1.5–2.0 mg cm^{-2}. LiR2032 half cells were assembled in a glove box filled with argon (Mikrouna, O_2, and $H_2O \leq 0.01$ ppm). The prepared electrode was used as anode material, and the lithium metal sheet was used as counter-electrode. 1 M $LIPF_6$ in a 50 : 50 (w/w) mixture

 © 2021 The Author(s). Published by the Royal Society of Chemistry

of dimethyl carbonate (DMC) and ethylene carbonate (EC) was used as the electrolytes. A CT2001A cell tester (Land, China) was used to perform Galvanostatic cycle stability within the potential range of 0.01–3.0 V (*vs.* Li^+/Li) and test rate performance at different current densities. Electrochemical impedance spectroscopy (EIS) tests ranged from 0.01 Hz to 100 kHz, and cyclic voltammetry (CV) studies were conducted at the CHI660E Electrochemical Workstation (CHI-Instrument).

Results and discussion

Due to the low electronic conductivity of natural molybdenite, it hinders the transport of ions and electrons. This enables natural molybdenite to adopt a reasonable and universal strategy to accelerate the transmission of charge carriers. Heterostructures were constructed to allow the formation of an internal E-field in the bulk MoS_2 to accelerate reaction kinetics and transport charge carriers. In theory, the strength of the electric field is crucial to the carrier transmission rate, and the bandgap difference of the components shows a positive linear relationship.[21–23] The natural molybdenite belongs to 2H MoS_2 with an indirect bandgap of about 1.17 eV and a low inherent electronic conductivity.[11] However, 1T MoS_2 has a metallic property with a bandgap difference of about 0 eV.[24] When the 1T phase was in contact with the 2H phase, a relatively strong electric field could be formed, providing rapid charge transfer dynamics (Fig. 1). Electrons move from the 2H MoS_2 at the high Fermi level to the 1T MoS_2 at the low Fermi level, and an internal electric field is generated to balance this transfer. The key is to transform part of the 2H phase *in situ* into 1T phase in natural molybdenite and construct 1T@2H MoS_2 heterostructures. To verify the heterostructure properties can enhance the electron migration rate, the powder electrical conductivity of 1T@2H MoS_2 was tested to be 10 S cm^{-1}. It showed more than 10^6 of the molybdenite concentrate and $\sim 4.5 \times 10^4$ times of the commercial MoS_2 (Table S2†).

Fig. 2 illustrates the new synthesis method of 1T@2H MoS_2 heterostructures with worm-like prepared from natural molybdenite *via* the expansion. The 1T@2H MoS_2 heterostructures

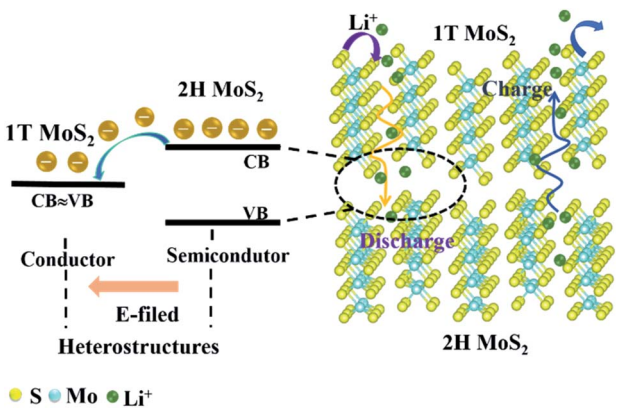

Fig. 1 Schematic of the internal E-field of the 1T@2H MoS_2 heterostructures.

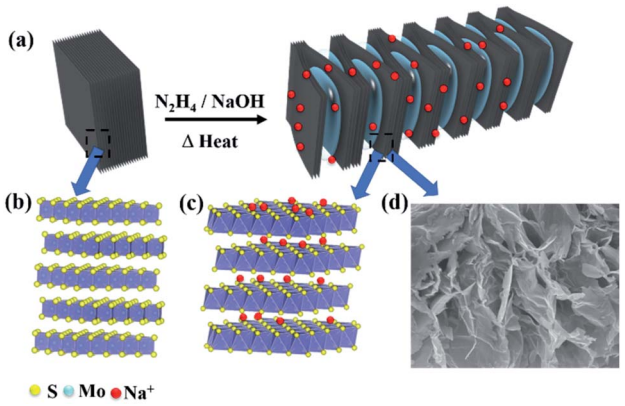

Fig. 2 (a) Schematic diagram of the preparation process of 1T@2H MoS_2 heterostructures with worm-like. (b) 2H MoS_2 crystal structure model. (c) 1T MoS_2 crystal structure model of Na^+ embedded 2H MoS_2. (d) Local FESEM image of 1T@2H MoS_2.

were caused by the synergistic effect of hydrazine hydrate and sodium hydroxide through insertion and expansion. Hydrazine and sodium hydroxide overcome the force between the MoS_2 layers to expand in a high-pressure and high-temperature environment. The redox rearrangement model can explain the formation of 1T@2H MoS_2 heterostructures. N_2H_4 was oxidized to $N_2H_5^+$ upon intercalation. Under heating conditions, $N_2H_5^+$ could be decomposed and gasified into N_2, NH_3, and H_2 because it was not heat-resistant.[25,26] These gases overcame the van der Waals force between MoS_2 layers to expand, significantly boosting the volume of MoS_2 and forming many pores. Simultaneously, MoS_2 was reduced and negatively charged, and Na^+ was first adsorbed on the crystal surface. The van Waals forces of the first two layers continued to weaken and penetrated to the next layer to form $Na_xMoS_2^+$, increasing the electronic energy in the MoS_2 layer. This structural change from the 2H to 1T phase is crucial. Note that the transformation of the trigonal prismatic coordinated 2H MoS_2 into the octahedral coordinated 1T MoS_2 could effectively improve the electronic conductivity of the MoS_2. In addition, sodium hydroxide has another vital role in removing other impurities in molybdenite concentrate components to obtain high purity MoS_2. The expansion method has a low cost and simple process for the scalable production of 1T@2H MoS_2 heterostructures.

The crystal phase and structure of molybdenite concentrate and 1T@2H MoS_2 samples were detected by XRD and Raman (Fig. 3). As shown in Fig. 3a, the prominent diffraction peaks of molybdenite concentrate are at $2\theta = 14.47°$, 32.71° and 60.18° corresponding to the (002), (100) and (110) crystal planes of 2H MoS_2 (PDF: 65-0160), respectively. Talc (PDF: 83-1768) and quartz (PDF: 75-0443) are also exist with molybdenite concentrate. Through XRD semi-quantitative analysis, the purity of molybdenite concentrate is about 78.51%. After expansion, the impurity phase disappeared, and the characteristic peaks ($2\theta = 14.50°$) of MoS_2 shifted to a high angle, which was attributed to the production of 1T MoS_2.[27,28] A new peak appeared at a low angle of $2\theta = 7.26°$, corresponding to the (001) crystal plane, with Na^+ insertion to form Na_xMoS_2.[29,30] The characteristic peak

© 2021 The Author(s). Published by the Royal Society of Chemistry

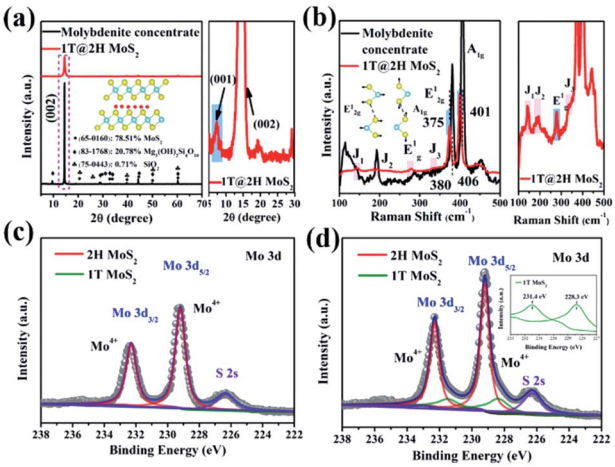

Fig. 3 (a) XRD patterns of molybdenite concentrate and 1T@2H MoS_2. (b) Raman patterns of molybdenite concentrate and 1T@2H MoS_2. (c) Mo 3d spectra of molybdenite concentrate. (d) Mo 3d spectra of 1T@2H MoS_2.

intensity of 1T@2H MoS_2 is lower than that of molybdenite concentrate, indicating the synergistic effect of hydrazine and sodium hydroxide expanded successfully natural molybdenite.[20,31] The XRF test (Table S3†) further verified that after the expansion of molybdenite concentrate, the content of Mo and S elements increased significantly, while other impurities decreased greatly. Meanwhile, the content of 2.52% Na_2O appeared, proving that Na^+ was embedded in MoS_2 layers, causing the transition from the 2H to the 1T phase. According to different process conditions such as reaction temperature, time, and sodium hydroxide concentration, 1T@2H MoS_2 was prepared and subjected to an XRD test (Fig. S1†). The structure shows that the best expansion process is a reaction at 150 °C for 24 h with 25 mol L^{-1} sodium hydroxide.

Raman spectroscopy is a sensitive method to identify the generation of 1T MoS_2.[28] Fig. 3b shows that molybdenite concentrate has two significant characteristic peaks at 380 cm^{-1} (E^1_{2g}, Mo–S in-plane vibration mode) and 406 cm^{-1} (A^1_g, Mo–S out-of-plane vibration mode).[32] After expansion, in addition to E^1_{2g} (375 cm^{-1}) and A^1_g (401 cm^{-1}), a series of additional Raman signals appeared at 144 cm^{-1} (J_1), 197 cm^{-1} (J_2), 279 cm^{-1} (E^1_g), and 332 cm^{-1} (J_3).[33–35] The E^1_g band is associated with the octahedral coordination of Mo in 1T MoS_2.[33] These new characteristic peaks prove the formation of 1T MoS_2. Remarkably, compared with molybdenite concentrate, the characteristic fingerprinting peaks of MoS_2 after expansion slightly shifted to lower wavenumbers, indicating the formation amount 1T@2H MoS_2 heterostructures. The red-shift of the Raman spectrum provides adequate evidence for the heterostructures interaction between 1T and 2H MoS_2.[11,36,37] UV-Vis absorption spectra tested the molybdenite concentrate and 1T@2H MoS_2 prepared under different conditions, and the results are shown in Fig. S2†. In contrast, after the expansion of molybdenite concentrate, the dispersion was gray, and the exciton peaks at A and B were not apparent, which also proved the existence of 1T MoS_2.[38,39] Moreover, XPS semi-quantitative method was used to verify that the 1T phase was produced in 1T@2H MoS_2, and the relative content ratio of the 2H and 1T phase was determined by analysis.[34] AS shown in Fig. 3c and d, the Mo $3d_{5/2}$ and Mo $3d_{3/2}$ peaks for 1T@2H MoS_2 exhibit a shift of 0.1 eV to lower binding energy, attributed to the production of the 1T phase.[15,34] In the Mo 3d region, Mo^{4+} $3d_{5/2}$ and Mo^{4+} $3d_{3/2}$ are at 229.2 eV and 232.3 eV, respectively (calibrated with C 1s peak at 284.5 eV), which belong to 2H MoS_2.[15,40] The corresponding peak of Mo in 1T MoS_2 is located at a lower position near 228.3 and 231.4 eV.[29,40] The same trend exists in the S 2p XPS area (Fig. S3†). By calculating the peak area of Mo 3d, the 1T phase composed about 20% in the 1T@2H MoS_2.

According to XPS analysis, it can be concluded that the change of molybdenite concentrate and 1T@2H MoS_2 are originated from the electronic migration synergistic effect between 1T and 2H phase heterostructures.

FESEM and TEM were used to examine the morphology and structure of the samples. In particular, HRTEM can effectively prove the existence of 1T MoS_2. As a comparison, natural molybdenite is a compact lamellar accumulation structure with a thickness of fewer than 5 μm in most cases (Fig. S4(a–c)†), accompanied by its average volume diameter of 42 μm (Fig. S4d†). The 1T@2H MoS_2 appears worm-like with the interlayer spacing opening and the formation of multilevel pore structures on the lamellar surface (Fig. 3a–c). This increases the contact area between the electrode materials and the electrolyte. Worm-like structures are beneficial for accommodating the enlargement of volume during the Li^+ intercalation owing to enough void space between neighboring sheets. The nitrogen adsorption–desorption isotherm results (Fig. S5†) validated that 1T@2H MoS_2 has a high specific surface area and pore volume, respectively 46.91 m^2 g^{-1} and 0.145 cm^3 g^{-1}, 38 and 29 times that of molybdenite concentrate. Moreover, the pore size distribution results showed that abundant micropores of 1T@2H MoS_2 mainly concentrated at 2 nm by Barrett–Joyner–Halenda (BJH) analysis (inset of Fig. S5b†). 1T@2H MoS_2 has a high specific surface area and rich micropores, which is beneficial to accelerate electrolyte penetration and provide more Li-ion channels. The FSSEM images of 1T@2H MoS_2 prepared under different process conditions are shown in Fig. S6–S8.† When the oil bath was at 150 °C for 24 h with 25 mol L^{-1} sodium hydroxide, the expansion was the most sufficient. This is consistent with the XRD conclusions. The TEM image (Fig. 4d) reveals that several micro-sized few layers of MoS_2 constructed the bulky worm-like 1T@2H MoS_2 with many holes on the surface. HRTEM image in Fig. 4e, the interlayer spacing of MoS_2 at the defect sites increased in varying degrees. The interlayer spacing is 0.55–0.78 nm, suggesting Li^+ is easier to diffuse into the expanded interlayer with vacancies.[41] The layer spacing is consistent with XRD results. HRTEM images (Fig. 4f) showed that intermittent lattice fringes appeared on the MoS_2 sheets, indicating the existence of S defects. The abundant defects could also realize the 3D diffusion of lithium ions.[42,43] Fig. 4g and h displayed two amplified HRTEM images intercepted from Fig. 4f, showing some hexagonal lattice regions with 2H MoS_2 and triangular lattice regions 1T MoS_2, which directly proved the existence of 1T

 © 2021 The Author(s). Published by the Royal Society of Chemistry

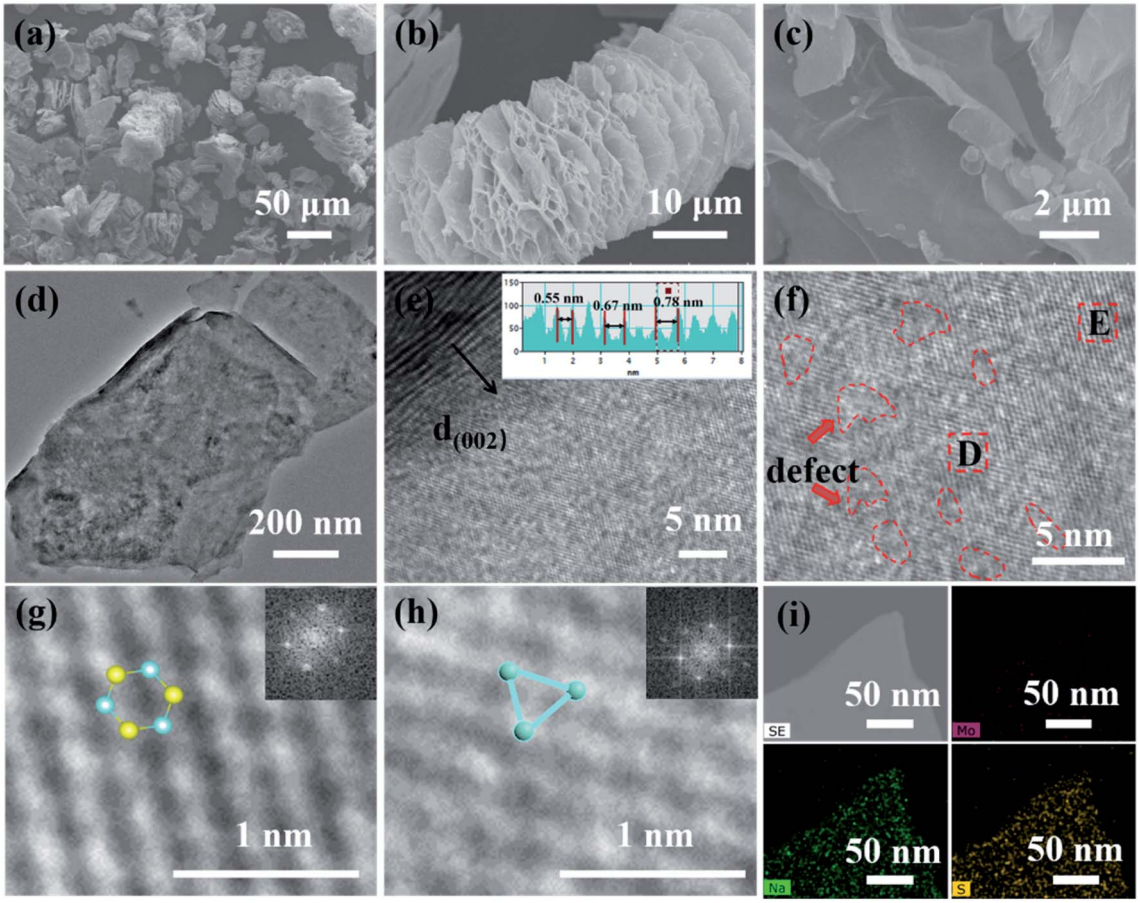

Fig. 4 (a–c) SEM images of 1T@2H MoS_2. (d) TEM, and (e–h) high-resolution TEM images of 1T@2H MoS_2. The insets in (g) and (h) are atomic models and fast-Fourier-transform patterns for 2H MoS_2 and 1T MoS_2. The illustrations in (g) and (h) are the atomic models of 2H MoS_2 and 1T MoS_2. (i) STEM-EDX element mapping, Mo (red), Na (yellow), S (blue), respectively.

MoS_2.[44] The illustrations in the upper right corner of Fig. 4g and h were obtained by Fourier transformation of the D and H regions, corresponding to 2H and 1T phases, respectively. Fig. 4i, STEM-EDX confirmed that Mo, S, and Na were uniformly distributed on the 1T@2H MoS_2 sheets, which further ensured Na^+ insert into the MoS_2 interlayer.

The metallic 1T MoS_2 with high electron conductivity formed *in situ* could include an internal E-field with 2H MoS_2 to accelerate the transport of lithium ions and electrons. Fig. 5a shows the initial three cyclic voltammograms (CV) curves of the 1T@2H MoS_2 heterostructures anode at a scan rate of 0.2 mV s^{-1} to explore the occurred reaction's details. Molybdenite concentrate has a similar changing trend as reference material (Fig. S9a†). Typical redox reaction characteristics were observed in the CV curve of MoS_2, which exhibited two reduction peaks at ~0.8 V and ~0.4 V in the first cathodic scan. The former represents Li^+ embedded in MoS_2 to form Li_xMoS_2 (*i.e.*, $MoS_2 + xLi^+ \rightarrow Li_xMoS_2$), while the latter is attributed to Li^+ embedded in Li_xMoS_2 transform into metallic Mo particles and Li_2S (*i.e.*, $Li_xMoS_2 + (4 - x)Li^+ + (4 - x)e^- \rightarrow Li_2S + Mo$).[45,46] In addition, Li_2S and S from a reversible redox couple at around 1.9/2.3 V.[47,48] It is worth noting that the coincidence degree of the first three cycles of 1T@2H MoS_2 is better than that of natural molybdenite, suggesting good cycling reversibility.[49]

As a comparison, the 1T@2H MoS_2 delivers a high discharging capacity of 1036 mA h g^{-1}, which is much higher than that of molybdenite concentrate (762 mA h g^{-1}), at a current density of 100 mA g^{-1} (Fig. 5b and S9b†). As shown in Fig. S9c†, 1T@2H MoS_2 is significantly shortened on the ~1.1 V platform, indicating that part of the triangular prism 2H phase is transformed into the octahedral 1T phase because this platform corresponds to Li^+ embedded MoS_2 to form Li_xMoS_2.[50,51] Compared with the discharge platform of MoS_2 prepared under different conditions, sample C_{20} showed a relatively higher platform, indicating that it has better lithium-ion diffusion kinetics (Fig. S9(d–f)†).[41] Fig. 5c, 1T@2H MoS_2 has excellent rate performance (727 mA h g^{-1}) and is superior over molybdenite concentrate, especially at 1 A g^{-1} high current density. When the current density is back to 100 mA g^{-1}, the capacity can be recovered to 927 mA h g^{-1} again, indicating that the electrode materials can achieve rapid charge–discharge performance. The 1T@2H MoS_2 has a worm-like structure and expanded layer spacing, which increases the specific capacity and effectively alleviates the capacity attenuation caused by the volume expansion effect in the cycle process. As shown in Fig. 5d, within

© 2021 The Author(s). Published by the Royal Society of Chemistry

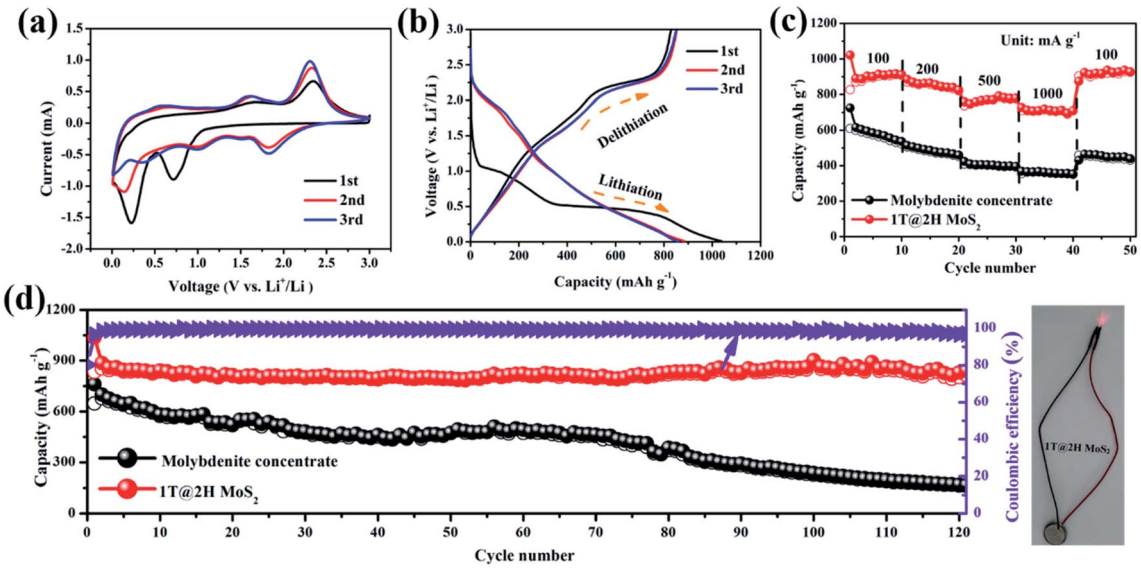

Fig. 5 Electrochemical performance: (a) CV curve of 1T@2H MoS_2; (b) charge and discharge curve of 1T@2H MoS_2; (c) rate capabilities of 1T@2H MoS_2; (d) cyclic performance of molybdenite concentrate and 1T@2H MoS_2.

120 cycles, the capacity of 1T@2H MoS_2 decays by only 0.04% per cycle after the second cycle compared to the capacity of molybdenite concentrate of 169 mA h g^{-1}. Hence, 1T@2H MoS_2 has excellent cycling stability performance. Similarly, after 120 cycles, the molybdenite concentrate electrode suffered damage severely, while the 1T@2H MoS_2 electrode maintained a fine integrity structure, which further proved that the heterostructures material has better structural stability (Fig. S10(a and b)†). In addition, after 120 cycles, the separator color of the 1T@2H MoS_2 electrode is relatively lighter, which indicates that the electrode can inhibit the shuttle of polysulfide and more effectively maintain electrode stability (Fig. S10c†). After 482 cycles, 1T@2H MoS_2 still has a 788 mA h g^{-1}, even at the lowest specific capacity of 311 mA h g^{-1}, which is close to the theoretical capacity of commercial graphite (Fig. S11†). Based on the comprehensive comparison in Table S4†, the 1T@2H MoS_2 heterostructures deliver high specific capacity and long cycle life among the most reported works for LIBs. The rate performance and cycling stability of 1T@2H MoS_2 prepared under other conditions are shown in Fig. S12 and S13†.

To better understand excellent electrochemical performance, a series of CV at scan rates 0.1–0.8 mV s^{-1} (Fig. 6a and d) and EIS measurements (Fig. 6e and f) were used to study the reaction kinetics of the 1T@2H MoS_2 electrode. In general, the battery capacity can be divided into two parts: the diffusion-controlled battery capacity and the surface pseudocapacitance.[49] Compared with the capacitance contribution, the battery contribution behaviour (*i.e.*, insertion mechanism) is a process that takes place in the bulk of the electrode and is not conducive to long cycle life. The charge storage mechanism is evaluated according to the formula: $i = av^b$, and the parameter b values are determined by $\log(v) \sim \log(i)$.[52] When the value of b is close to 1 or more than 1, indicating capacitive-controlled plays a leading role, whereas the b-value approaches 0.5, suggesting that diffusion-controlled are dominant in the electrochemical reactions.[53] Fig. 6b shows the b value are 0.89 and 1.16 for anodic and cathodic peaks, respectively, suggesting a significant capacitive contribution. The b values of 1T@2H MoS_2 are larger than that of molybdenite concentrate (Fig. S15b†), which means faster reaction kinetics. According to eqn (1),[44,54] the capacitance contribution ratio can be quantified at a given scanning rate.

$$i = k_1\nu + k_2\nu^{1/2} \tag{1}$$

where k_1 and k_2 are constants at a given voltage. In Fig. 6c, the contribution rate of pseudocapacitance is 72.3% at 0.2 mV s^{-1}. As the scanning rate increases, the contribution rate of pseudocapacitance increases to a maximum of 82.9% at 0.8 mV s^{-1} in Fig. 6d. The overwhelming pseudocapacitive behavior leads to fast lithiation/delithiation processes in the 1T@2H MoS_2 electrode, which is attributed to the internal E-field between 2H MoS_2 and 1T MoS_2.[49,52] Simultaneously, at the same scanning rate, the pseudocapacitive contribution rate of molybdenite concentrate is relatively lower, indicating that the molybdenite concentrate has a relatively slow lithium-ion reaction kinetics (Fig. S14(c and d)†). To further explore the heterostructure materials' kinetic properties and electrochemical performance, electrochemical impedance spectroscopy (EIS) was carried out to measure molybdenite concentrate and 1T@2H MoS_2 electrodes shown in Fig. 6e and f. By fitting the equivalent circuit (inset in Fig. 6e), the ohmic resistance (R_e) and charge transfer resistance (R_{ct}) of the electrode materials are shown in Table S5†. Compared with molybdenite concentrate in the Nyquist plots (Fig. 6e), 1T@2H MoS_2 has a lower charge transfer resistance, indicating a faster charge transfer rate. To calculate the diffusion coefficient (D) value, the relationship between Z' and $\omega^{-1/2}$ in the low-frequency region is plotted and fitted based on eqn (2).[14] The results are shown in Fig. 6f.

 © 2021 The Author(s). Published by the Royal Society of Chemistry

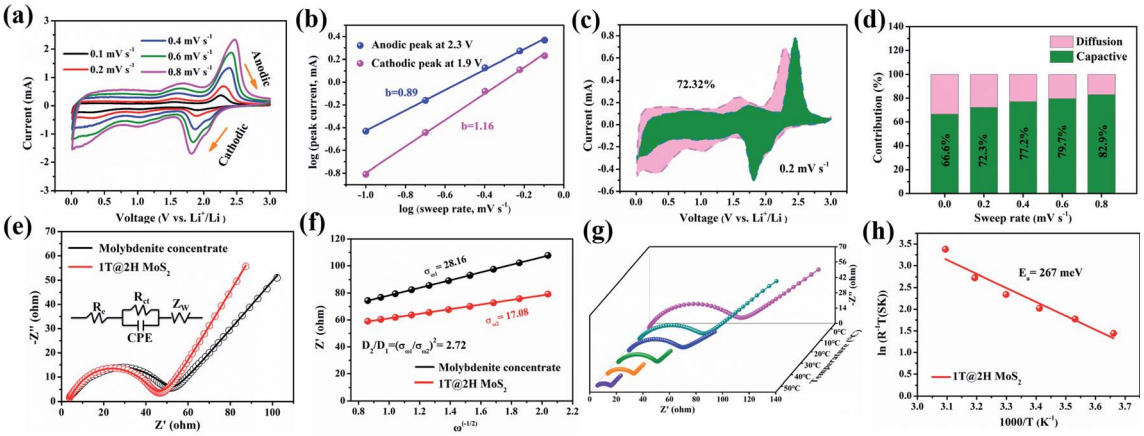

Fig. 6 Electrochemical kinetic analysis diagram: (a) CV curves of scanning rate from 0.1 to 0.2 mV s^{-1}; (b) log(*i*) *vs.* log(*v*) plots at oxidation and reduction state; (c) capacitance and diffusion control contribute to the CV curve at 0.2 mV s^{-1}; (d) the contribution ratio of pseudocapacitive and diffusion-controlled contribution of the1T@2H MoS_2 electrode at different scan rates; (e) EIS Nyquist plots of molybdenite concentrate and 1T@2H MoS_2 (the inset of equivalent circuit); (f) the relationship between Z' and $\omega^{-1/2}$ for molybdenite concentrate and 1T@2H MoS_2 electrodes. (g) Temperature-dependent Nyquist plots of 1T@2H MoS_2; (h) reciprocal bulk and interface impedance as a function of the reciprocal temperature of 1T@2H MoS_2.

$$Z' = R_e + R_{ct} + \sigma\omega^{-1/2} \quad (2)$$

Then, the Warburg factor σ obtained by fitting is substituted into eqn (3)[50] to calculate the D value.

$$D = R^2T^2/2n^4F^4C^2\sigma^2A^2 \quad (3)$$

where R, T, n, F, A, and C are the gas constant, absolute temperature, the transfer electrons, the Faraday constant, Warburg coefficient, the area of the electrode, and the Li^+ concentration in the electrode, respectively. These σ and D values of electrode materials are also listed in Table S5†. The table shows that the diffusion coefficient for 1T@2H MoS_2 is 2.7 times that of natural molybdenite, verifying the enhanced kinetics of Li^+ intercalation/deintercalation for 1T@2H MoS_2 heterostructures. The faster charge transfer and higher diffusion coefficient ensure excellent cycling stability and magnification performance for the 1T@2H MoS_2 heterostructures electrode. To further explore reaction dynamics, we performed a temperature-dependent EIS measurement to study the charge transfer resistance and activation energy E_a in Fig. 4g and h. The charge transfer resistance values at different temperatures are shown in Tables S6 and S7†. The E_a is calculated by the Arrhenius eqn (4):[49,55]

$$\sigma T = A\exp(-E_a/k_BT) \quad (4)$$

where σ, T, A, E_a, and k_B are the ionic conductivity, absolute temperature, a constant, activation energy for ion transport, and the Boltzmann constant, respectively. The activation energy E_a of 1T@2H MoS_2 is calculated as 267 meV (Fig. 6h), lower than the 320 meV of natural molybdenite (Fig. S15†), suggesting a lower charge transfer energy barrier, which benefits capacitor energy storage, and Li^+ can be transferred quickly in the whole-cell. Hence, it has a good lithium storage performance.

Conclusions

In conclusion, we used an innovative expansion method to construct worm-like 1T@2H MoS_2 heterostructures *in situ* on natural molybdenite, which could effectively improve lithium-ion storage and reaction performance kinetics. With the advantage of the internal E-field, the 1T@2H MoS_2 heterostructures electrode displays a high reversible capacity of 788 mA h g^{-1} at a current density of 0.1 A g^{-1} over 485 cycles (corresponding to 92% capacity retention of the second cycle). More importantly, the 1T@2H MoS_2 heterostructures electrode exhibits high rate capability performance (727 mA h g^{-1} at 1 A g^{-1}) for lithium-ion batteries. Electrochemical kinetic analysis shows that 1T@2H MoS_2 has lower charge transfer resistance and activation energy, and pseudocapacitance dominates the storage mechanism of lithium-ions. These fast dynamics aid high magnification and high capacity capabilities. This work not only solves the significant challenges of the low inherent electrical conductivity of MoS_2 but also provides a feasible way to use low-cost molybdenite concentrate as raw materials for high-performance next-generation commercial energy storage devices.

Conflicts of interest

The authors declare no competing financial interest.

Acknowledgements

This work was supported by the Cooperation Foundation of Key Laboratory of Mineralogy and Metallogeny, Chinese Academy of Sciences, Guangzhou Institute of Geochemistry (2020B1212060055), the National Natural Science Foundation of China (52002361).

© 2021 The Author(s). Published by the Royal Society of Chemistry

References

1 W. T. Li, X. W. Guo, Y. Lu, L. Wang, A. L. Fan, M. L. Sui and H. J. Yu, *Energy Storage Materials*, 2017, **7**, 203–208.

2 S. J. Li, H. H. Tang, P. Ge, F. Jiang, J. H. Zhou, C. Y. Zhang, H. S. Hou, W. Sun and X. B. Ji, *ACS Appl. Mater. Interfaces*, 2018, **10**, 6378–6389.

3 L. L. Wang, Q. F. Zhang, J. Y. Zhu, X. D. Duan, Z. Xu, Y. T. Liu, H. G. Yang and B. G. Lu, *Energy Storage Materials*, 2018, **16**, 37–45.

4 J. Shao, Q. T. Qu, Z. M. Wan, T. Gao, Z. C. Zuo and H. H. Zhe, *ACS Appl. Mater. Interfaces*, 2015, **7**, 22927–22934.

5 K. K. Liu, W. J. Zhang, Y. H. Lee, Y. C. Lin, M. T. Chang, C. Y. Su, C. S. Chang, H. Li, Y. M. Shi, H. Zhang, C. S. Lai and L. J. Li, *Nano Lett.*, 2012, **12**, 1538–1544.

6 J. X. Guo, H. F. Zhu, Y. F. Sun, L. Tang and X. Zhang, *J. Mater. Chem. A*, 2016, **4**, 4783–4789.

7 H. Y. Wang, B. Y. Wang, D. Wang, L. Lu, J. G. Wang and Q. C. Jiang, *RSC Adv.*, 2015, **5**, 58084–58090.

8 Y. C. Lin, D. O. Dumcenco, Y. S. Huang and K. Suenga, *Nat. Nanotechnol.*, 2014, **9**, 391–396.

9 Y. Katagiri, T. Nakamura, A. Ishii, C. Ohata, M. Hasegawa, S. Katsumoto, T. Cusati, A. Fortunelli, G. Iannaccone, G. Fiori, S. Roche and J. Haruyama, *Nano Lett.*, 2016, **16**, 3788–3794.

10 Y. Nagamine, J. Sato, Y. Qian, T. Inoue, T. Nakamura, S. Maruyama, S. Katsumoto and J. Haruyama, *Appl. Phys. Lett.*, 2020, **117**, 043101.

11 C. Z. Zhang, F. Han, F. Wang, Q. D. Liu, D. W. Zhou, F. Q. Zhang, S. H. Xu, C. L. Fan, X. K. Li and J. S. Liu, *Energy Storage Materials*, 2020, **24**, 208–219.

12 D. Sun, D. L. Ye, P. Liu, Y. G. Tang, J. Guo, L. Z. Wang and H. Y. Wang, *Adv. Energy Mater.*, 2018, **8**, 1702383.

13 S. C. Li, P. Liu, X. B. Huang, Y. G. Tang and H. Y. Wang, *J. Mater. Chem. A*, 2019, **7**, 10988–10997.

14 J. Bai, B. C. Zhao, J. F. Zhou, Z. T. Fang, K. Z. Li, H. Y. Ma, J. M. Dai, X. B. Zhu and Y. P. Sun, *ChemElectroChem*, 2019, **6**, 1930–1938.

15 D. Sun, D. Huang, H. Y. Wang, G. L. Xu, X. Y. Zhang, R. Zhang, Y. G. Tang, D. Abd EI-Hady, W. Alshitari, A. S. AL-Bogami, K. Amine and M. H. Shao, *Nano Energy*, 2019, **61**, 361–369.

16 Y. Zhou, Y. Liu, W. X. Zhao, R. M. Xu, D. H. Wang, B. J. Li, X. Zhou and H. Shen, *Electrochim. Acta*, 2016, **211**, 1048–1055.

17 Z. D. Lei, L. Q. Xu, Y. L. Jiao, A. J. Du, Y. Zhang and H. J. Zhang, *Small*, 2018, **14**, 1704410.

18 S. Das, G. Swain and K. Parida, *Mater. Chem. Front.*, 2021, **5**, 2143–2172.

19 G. Eda, H. Yamaguchi, D. Voiry, T. Fujita, M. W. Chen and M. Chhowalla, *Nano Lett.*, 2011, **11**, 5111–5116.

20 A. Ejigu, L. A. Kinloch, E. Prestat and R. A. W. Dryfe, *J. Mater. Chem. A*, 2017, **5**, 11316–11330.

21 Y. Zheng, T. F. Zhou, C. F. Zhang, J. F. Mao, H. K. Liu and Z. P. Guo, *Angew. Chem., Int. Ed.*, 2016, **55**, 3408–3413.

22 J. J. Deng, X. L. Yu, X. Y. Qin, D. Zhou, L. H. Zhang, H. Duan, F. Y. Kang, B. H. Li and G. X. Wang, *Adv. Energy Mater.*, 2019, **9**, 1803612.

23 C. Z. Zhang, F. Han, J. M. Ma, Z. Li, Z. Li, F. Q. Zhang, S. H. Xu, H. B. Liu, X. K. Li, J. S. Liu and A. H. Lu, *J. Mater. Chem. A*, 2019, **7**, 11771–11781.

24 X. F. Qian, J. W. Liu, L. Fu and J. Li, *Science*, 2014, **346**, 1344–1347.

25 N. D. Scott, J. F. Walker and V. L. Hansley, *J. Am. Chem. Soc.*, 1936, **58**, 2442.

26 J. Zheng, H. Zhang, S. H. Dong, Y. P. Liu, C. T. Nai, H. S. Shin, H. Y. Jeong, B. Liu and K. P. Loh, *Nat. Commun.*, 2014, **5**, 2995.

27 Y. F. Yu, G. H. Nam, Q. Y. He, X. J. Wu, K. Zhang, Z. Z. Yang, J. Z. Wang, H. Li , X. Huang, B. Li, Q. H. Xiong, Q. Zhang, Z. Liu , L. Gu, Y. H. Du, W. Huang and H. Zhang, *Nat. Chem.*, 2018, **10**, 638–643.

28 M. A. Lukowski, A. S. Daniel, F. Meng, A. Forticaux, L. S. Li and S. Jin, *J. Am. Chem. Soc.*, 2013, **135**, 10274–10277.

29 N. Joseph, P. M. Shafi and A. C. Bose, *New J. Chem.*, 2018, **42**, 12082–12090.

30 K. Chang, X. Hai, H. Pang, H. B. Zhang, L. Shi, G. G. Liu, H. M. Liu, G. X. Zhao, M. Li and J. H. Ye, *Adv. Mater.*, 2016, **28**, 10033–10041.

31 G. S. Bang, K. W. Nam, J. Y. Kim, J. Y. Kim, J. Shin, J. W. Choi and S. Y. Choi, *ACS Appl. Mater. Interfaces*, 2014, **6**, 7084–7089.

32 D. S. Kong, H. T. Wang, J. J. Cha, M. Pasta, K. J. Koski, J. Yao and Y. Cui, *Nano Lett.*, 2013, **13**, 1341–1347.

33 H. M. Fan, R. Wu, H. Y. Liu, X. Yang, Y. F. Sun and C. Chen, *J. Mater. Sci.*, 2018, **53**, 10302–10312.

34 X. Y. Chen, Z. M. Wang, Y. Z. Wei, X. Zhang, Q. H. Zhang, L. Gu, L. J. Zhang, N. L. Yang and R. B. Yu, *Angew. Chem., Int. Ed.*, 2019, **58**, 17621–17624.

35 S. J. R. Tan, I. Abdelwahab, Z. J. Ding, X. X. Zhao, T. S. Yang, G. Z. J. Loke, H. Lin, I. Verzhbitskiy, S. M. Poh, H. Xu, C. T. Nai, W. Zhou, G. Eda, B. H. Jia and K. P. Loh, *J. Am. Chem. Soc.*, 2017, **139**, 2504–2511.

36 C. T. Zhao, C. Yu, B. Qiu, S. Zhou, M. D. Zhang, H. W. Huang, B. Q. Wang, J. J. Zhao, X. L. Sun and J. S. Qiu, *Adv. Mater.*, 2018, **30**, 1702486.

37 Y. Y. Wang, W. P. Kang, D. W. Cao, M. H. Zhang, Z. X. Kang, Z. Y. Xiao, R. M. Wang and D. F. Sun, *J. Mater. Chem. A*, 2018, **6**, 4776–4782.

38 S. Reshmi, M. V. Akshaya, B. Satpati, P. K. Basu and K. Bhattacharjee, *Nanotechnology*, 2018, **29**, 205604.

39 X. M. Geng, W. W. Sun, W. Wu, B. Chen, A. Al-Hilo, M. Benamara, H. L. Zhu, F. Watanabe, J. B. Cui and T. P. Chen, *Nat. Commun.*, 2016, **7**, 10672.

40 T. Xiang, Q. Fang, H. Xie, C. Q. Wu, C. D. Wang, Y. Zhou, D. B. Liu, S. M. Chen, A. Khalil, S. Tao, Q. Liu and L. Song, *Nanoscale*, 2017, **9**, 6975–6983.

41 K. Yao, Z. W. Xu, J. F. Huang, M. Ma, L. C. Fu, X. T. Shen, J. Li and M. S. Fu, *Small*, 2019, **15**, 1805405.

42 Y. Yin, J. C. Han, Y. M. Zhang, X. H. Zhang, P. Xu, Q. Yuan, L. Samad, X. J. Wang, Y. Wang, Z. H. Zhang, P. Zhang,

© 2021 The Author(s). Published by the Royal Society of Chemistry

X. Z. Cao, B. Song and S. Jin, *J. Am. Chem. Soc.*, 2016, **138**, 7965–7972.
43 D. Su, S. X. Dou and G. X. Wang, *Adv. Energy Mater.*, 2014, **5**, 1401205.
44 W. Ye, F. F. Wu, N. X. Shi, H. Zhou, Q. Q. Chi, W. H. Chen, S. Y. Du, P. Gao, H. B. Li and S. L. Xiong, *Small*, 2019, **16**, 1906607.
45 Z. Y. Li, A. Ottmann, T. Zhang, Q. Sun, H. P. Meyer, Y. Vaynzof, J. H. Xiang and R. Klingeler, *J. Mater. Chem. A*, 2017, **5**, 3987–3994.
46 F. Y. Xiong, Z. Y. Cai, L. B. Qu, P. F. Zhang, Z. F. Yuan, O. K. Asare, W. W. Xu, C. Lin and L. Q. Mai, *ACS Appl. Mater. Interfaces*, 2015, **7**, 12625–12630.
47 J. W. Zhou, J. Qin, X. Zhang, C. S. Shi, E. Z. Liu, J. J. Li, N. Q. Zhao and C. N. He, *ACS Nano*, 2015, **9**, 3837–3848.
48 X. X. Zuo, K. Chang, J. Zhao, Z. Z. Xie, H. W. Tang, B. Li and Z. R. Chang, *J. Mater. Chem. A*, 2016, **4**, 51–58.
49 X. Y. Li, K. K. Li, S. C. Zhu, K. Fan, L. L. Lyu, H. M. Yao, Y. Y. Li, J. L. Hu, H. T. Huang, Y. W. Mai and J. B. Goodenough, *Angew. Chem., Int. Ed.*, 2019, **58**, 6239–6243.
50 J. Bai, B. C. Zhao, J. F. Zhou, J. G. Si, Z. T. Fang, K. Z. Li, H. Y. Ma, J. M. Dai, X. B. Zhu and Y. P. Sun, *Small*, 2019, **15**, 1805420.
51 Y. C. Jiao, A. Mukhopadhyay, Y. Ma, L. Yang, A. M. Hafez and H. L. Zhu, *Adv. Energy Mater.*, 2018, **8**, 1702779.
52 J. Bai, B. C. Zhao, S. Lin, K. Z. Li, J. F. Zhou, J. M. Dai, X. B. Zhu and Y. P. Sun, *Nanoscale*, 2020, **12**, 1144–1154.
53 M. M. Yin, X. T. Feng, D. Zhao, Y. Zhao, H. S. Li, W. Zhou, H. B. Liu, X. P. Bai, H. X. Wang, C. H. Feng and Q. Z. Jiao, *ACS Sustainable Chem. Eng.*, 2019, **7**, 6122–6130.
54 Y. J. Fang, D. Y. Luan, Y. Chen, S. Y. Gao and X. W. Lou, *Angew. Chem., Int. Ed.*, 2020, **59**, 7178–7183.
55 G. Barik and S. Pal, *Adv. Theory Simul.*, 2020, **3**, 2000157.

© 2021 The Author(s). Published by the Royal Society of Chemistry